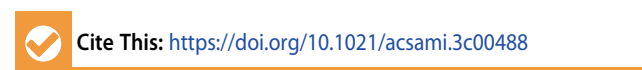


www.acsami.org Research Article

Copper Cobalt Selenide as a Bifunctional Electrocatalyst for the Selective Reduction of CO₂ to Carbon-Rich Products and Alcohol Oxidation

Apurv Saxena, Shubhender Kapila, Julia E. Medvedeva, and Manashi Nath*





ACCESS

Methanol

Formic acid

Vy RHE

Article Recommendations

Supporting Information

Actic acid,

Formic acid

Acetic acid

ABSTRACT: Copper cobalt selenide, CuCo₂Se₄, has been identified as an efficient catalyst for electrocatalytic CO₂ reduction, exhibiting high selectivity for carbon-rich and value-added products. Achieving product selectivity is one of the primary challenges for CO2 reduction reactions, and the catalyst surface plays a pivotal role in determining the reaction pathway and, more importantly, the intermediate adsorption kinetics leading to C1- or C2+-based products. In this research, the catalyst surface was designed to optimize the adsorption of the intermediate CO (carbonyl) group on the catalytic site such that its dwell time on the surface was long enough for further reduction to carbon-rich products but not strong enough for surface passivation and poisoning. CuCo₂Se₄ was synthesized through hydrothermal method, and the assembled electrode showed the electrocatalytic reduction of CO₂ at various applied potentials ranging from −0.1 to −0.9 V vs RHE. More importantly, it was observed that the CuCo₂Se₄-modified electrode could produce exclusive C2 products such as acetic acid and ethanol with 100% faradaic efficiency at a lower applied potential (-0.1 to -0.3 V), while C1 products such as formic acid and methanol were obtained at higher applied potentials (-0.9 V). Such high selectivity and preference for acetic acid and ethanol formation highlight the novelty of this catalyst. The catalyst surface was also probed through density functional theory (DFT) calculations, and the high selectivity for C2 product formation could be attributed to the optimal CO adsorption energy on the catalytic site. It was further estimated that the Cu site showed a better catalytic activity than Co; however, the presence of neighboring Co atoms with the residual magnetic moment on the surface and subsurface layers influenced the charge density redistribution on the catalytic site after intermediate CO adsorption. In addition to CO₂ reduction, this catalytic site was also active for alcohol oxidation producing formic or acetic acid from methanol or ethanol, respectively, in the anodic chamber. This report not only illustrates the highly efficient catalytic activity of CuCo₂Se₄ for CO₂ reduction with high product selectivity but also offers a proper insight of the catalyst surface design and how to obtain such high selectivity, thereby providing knowledge that can be transformative for the field.

KEYWORDS: CO₂ electroreduction, transition-metal selenides, acetic acid production, CO₂ utilization, alcohol oxidation

INTRODUCTION

Increased usage of fossil fuels and other nonrenewable resources to power this planet over the last several decades has caused environmental pollution, leading to major energy crisis. One of the primary byproducts of fossil fuel combustion and the resulting greenhouse gas is carbon dioxide. The rising levels of ${\rm CO}_2$ in the atmosphere have led to severe catastrophic effects, including erratic climatic changes and global warming. While carbon dioxide capture and sequestration can provide some

Received: January 12, 2023 Accepted: February 22, 2023



solution to this rising CO₂ level in the atmosphere, however, these technologies need to be complemented by the chemical conversion of atmospheric and stored CO2 to other carbonaceous products. Such processes can effectively reduce CO₂ levels in the atmosphere and, at the same time, close the carbon loop. Studies have been done using both heterogeneous and homogeneous routes for catalytic carbon dioxide reduction reaction (CO2RR)^{1,2} and other catalytic processes.^{3,4} The homogeneous route for CO2RR lacks scalability and leads to a low yield of product formation. In heterogeneous catalysis for CO2RR, different types of catalysts have been used like organometallic complexes, 5-7 metal electrodes 8,9 and metal chalcogenides. 10 Among the different methods for heterogeneous catalysis, electrochemical reduction of CO₂ has become a critical research area over the last few decades. One of the primary challenges for the advent of CO₂ electroreduction is the discovery of efficient CO2RR electrocatalysts that can not only reduce the reaction energy barrier leading to the facile transformation of CO2 but also lead to high selectivity in product formation.

Among the various catalysts that have been studied for CO₂ conversion, copper-based catalysts have been established to be very efficient in CO2 electrochemical reduction as different reduction products can be generated using different conditions with high selectivity. 11 Different aspects such as change in crystal faces, 12 morphology of the catalyst, 13 size of the catalyst particles, ¹⁴ and the valence state of the central metal atom ^{15,16} on the CO2RR catalytic activity have been investigated by various groups. However, although Cu-based catalysts have shown significant advances for CO2RR, the need to investigate the effect of transition-metal doping on the Cu-based compounds and, more importantly, the development of Cufree catalysts has become imminent for gaining fundamental insights into the structure-property correlation and formation of hydrocarbon and oxygenate products for these electrocatalysts.

One of the primary considerations for an electrocatalyst is the availability of accessible variable oxidation states of the catalytically active site. Cobalt is one such transition element which exhibits oxidation states from 0 to +4 which are readily accessible through facile electrochemical tuning. Co-based chalcogenides with variable compositions of transition-metal elements have already proven to be efficient electrocatalysts in many relevant processes like water splitting. However, during $\rm CO_2$ electroreduction, only the active site changes from $\rm Co^{2+}$ to $\rm Co^{1+}$ Metallic cobalt, $\rm ^{20}$ cobalt-based bimetallic compounds, $\rm ^{21,22}$ and cobalt oxide $\rm ^{23}$ have been studied for $\rm CO_2$ electrochemical conversion.

Regulation of activity and product selectivity has been achieved by varying the catalyst size in cobalt-based catalysts. ^{20,21,24,25} According to a study by Wannakao et al., Co metal has moderate CO binding strength as compared to other metals and thus has better catalytic performance for CO₂ electrochemical reduction. The presence of a cobalt center decreases the possibility of catalyst poisoning which occurs in metals like Pt and Rh and also decreases the applied potential compared to the metals with weak binding strength like Zn. ²⁶ Also, the presence of loosely bound d-electrons at the Co metal centers increases the electrical conductivity which enhances the activity toward CO2RR. ²³ Thus, cobalt-based catalysts have started gaining considerable attention for CO2RR due to their enhanced performance.

In this study, we have synthesized mixed transition-metal selenide, CuCo₂Se₄, through an efficient one-pot solvothermal synthesis method and studied the reactivity of this copper cobalt selenide for carbon dioxide reduction under ambient conditions. It was observed that the simultaneous presence of Cu and Co in the catalyst enhances the activity toward CO2RR in comparison to binary selenides. In addition, CuCo₂Se₄ exhibited a high degree of product selectivity, forming carbon-rich products such as acetic acid and ethanol exclusively at a low applied potential. We have also investigated the adsorption energy of intermediate CO on the catalyst surface and the corresponding changes of the surface electronic structure through density functional theory (DFT) calculations. These calculations showed that the CO adsorption energy was in the optimal range and better than that in binary Cu or selenides. Moreover, it also revealed that Cu has better selectivity and adsorption for intermediate CO compared to Co. Such a facile adsorption of intermediate CO on the catalyst surface along with the better electronic conductivity of the CuCo₂Se₄ matrix possibly leads to higher product selectivity at a low applied potential.

Experimental and Computational Methods. All chemicals were of analytical grade and used as purchased. CoCl₂·6H₂O, CuCl₂·2H₂O, SeO₂, N₂H₄·H₂O, and KOH were purchased from Sigma Aldrich. The carbon fiber paper (CFP) electrode and Nafion 115 membrane were purchased from Fuel Cell Store supplies.

Synthesis of CuCo₂Se₄ and Electrode Preparation. CuCo₂Se₄ was synthesized using hydrothermal synthesis. Specifically, 20 mmol of CuCl₂·2H₂O, 40 mmol of CoCl₂·6H₂O, and 40 mmol of SeO₂ were stirred together for 15 min in 15 mL of distilled water. 1.5 mL of N₂H₄·H₂O (hydrazine) was added dropwise while stirring to form a brown colloidal solution. This solution was then transferred into a Teflon-lined stainless steel autoclave and heated at 145 °C for 24 h, following which it was cooled to room temperature under ambient conditions. The final product was obtained using centrifugation. The crude powder was washed using absolute ethanol and then vacuum-dried overnight.

Catalyst ink was made by uniformly dispersing 5 mg of catalyst powder in 0.25 mL of 1% Nafion—ethanol solution using ultrasonication for 15 min. The CuCo_2Se_4 electrode was prepared by uniformly drop-casting the catalyst ink on a confined area. The area on the CFP substate was confined using a Teflon tape, and a geometric area of 0.283 cm² was left exposed for drop-casting the catalyst ink. The prepared electrode was dried overnight at room temperature.

Characterization of Catalyst. Powder X-ray Diffraction. Powder X-ray diffraction (PXRD) was used to identify the crystalline phase of the as-synthesized catalyst powder using a Philips X-Pert diffractometer utilizing CuK α (1.5418 Å) radiation. The PXRD pattern was collected by loading the powder on a Au-coated glass substrate.

Scanning Electron Microscopy and X-ray Photoelectron Spectroscopy. An FEI Helios NanoLab 600 FIB/FESEM system was used to observe the morphology of the product at an acceleration voltage of 10 kV and a working distance of 5 mm. To determine the composition via identifying the relative atomic ratio of elements present in the catalyst, EDS was done from the same SEM system. XPS was used to observe the oxidation states of the elements in the CuCo₂Se₄ catalyst using a KRATOS AXIS X-ray photoelectron spectrometer. Specific correction of Co, Cu, and Se binding energies was carried out by employing the C

1s binding energy of 284.5 eV. All XPS signals were measured from the pristine catalyst surface without any sputtering.

Electrochemical Activity for CO₂ Conversion. The electrochemical activity of the CuCo₂Se₄-modified electrode was measured in a two-compartment H-Cell with a CO₂-saturated 0.3 M NaHCO₃ solution. The two compartments were separated by a Nafion ion-exchange membrane. KCl-saturated AglAgCl was used as a reference electrode and was put in a cathodic compartment along with the working electrode. The carbon rod as a counter electrode was placed in the anodic compartment of the H-cell. CuCo₂Se₄-coated CFP prepared by the method described above was used as the working electrode. A catalyst loading of 1 mg cm⁻² was used for these studies.

Density Functional Theory Calculations. The electronic properties of the CuCo₂Se₄ (100) surface with and without CO were studied using first-principles density functional calculations, as implemented in the Vienna ab initio simulation package (VASP).^{27–30} The generalized gradient approximation (GGA) in the Perdew-Burke-Ernzerhof (PBE) form, 31,32 within the projector augmented-wave method was used. 33,34 The GGA + U method with an on-site Coulomb U = 0 or 6 eV for Co-d states and U = 0 or 4 eV for Cu-d states was used to study the electronic structure and magnetic properties of the CuCo₂Se₄ slab as well as the adsorption energy of CO at the Co 3 supercell with a vacuum region of 15 Å was used to create a surface model with CO adsorption. From a separate calculation, we find that the (100) cleavage energy for CuCo₂Se₄ saturates at less than 4 Å of vacuum separation so that the 15 Å vacuum layer is wide enough to prevent interaction between the surface atoms across that layer. The stoichiometry in the slab was kept identical to that of bulk with an integer number of formula units in the supercell to ensure the charge neutrality. The surface was not passivated to avoid additional species affect the calculated energetics related to the catalytic performance. The internal atomic positions for all structures were optimized using force and total energy minimization until the Hellmann-Feynman force on each atom was below 0.01 eV/Å. Brillouin zone sampling was done with Γ -centered Monkhorst-pack, with kmesh of at least $4 \times 4 \times 4$; the cutoff energy of 500 eV and Gaussian smearing were used.

RESULTS AND DISCUSSION

Characterization. Powder X-ray diffraction (PXRD) pattern collected from the as-synthesized powder showed a good match with the standard pattern of CuCo₂Se₄ (PDF No. 04-019-0997), confirming the formation of pure CuCo₂Se₄, as shown in Figure 1. As mentioned above, the PXRD pattern was collected by loading the sample on a Au-coated glass; hence, the diffraction peaks for polycrystalline Au were also observed at 38° and 82°, as marked in Figure 1. No other crystalline impurity phases were detected in the PXRD pattern. The diffraction peaks showed considerable broadening, indicating the formation of nanostructured grains. The Scherrer equation was used to calculate the size of such grains and the crystalline domain, following the standard procedure.³⁵ From the line broadening of the diffraction peaks, the approximate size of the crystalline domain was calculated to be 2.67 nm. The crystal structure of CuCo₂Se₄ has been reported previously from a single crystal structure solution.³⁶ According to the previous reports, $CuCo_2Se_4$ exhibits an AB_2X_4 (X = Chalcogen atom) spinel structure type, where A is a divalent cation occupying the tetrahedral layer and B is a trivalent cation occupying the fully

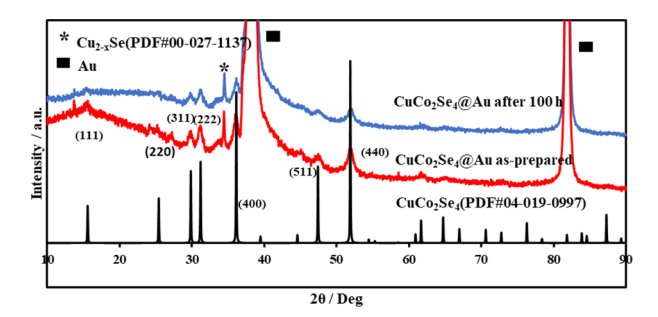


Figure 1. PXRD pattern of hydrothermally synthesized $CuCo_2Se_4$ compared with the standard $CuCo_2Se_4$ reference pattern (PDF # 04-019-0997).

occupied octahedral metal layer. The crystal structure shows that Co atoms were in the octahedral coordination sites and Cu atoms in the tetrahedral sites, where the unit cell has similar geometries for each of the Co/Cu atom. Also, the bond lengths between Co-Se and Cu-Se were found to be ~2.38 and 2.37 Å, respectively. The morphology of the hydrothermally synthesized powder was observed using SEM. In Figure 2, the SEM images depicted porous nanostructures having a size range of 100-200 nm. Such nanostructured morphology provides a large number of accessible active sites for CO2 and intermediate CO adsorption, which can get further reduced to desirable products. The oxidation states and chemical composition of the assynthesized powder were further investigated through XPS. The XPS peaks at 778 and 793 eV indicated the presence of Co in a Co-selenide bonding atmosphere, ³⁷ while peaks at 934 and 954 eV indicated the presence of copper selenide bonding.³⁸ The deconvoluted spectra of Co and Cu XPS peaks showed the presence of multiple oxidation states. As shown in Figure 2c, the deconvoluted Cu spectra shows peaks at 931.5 and 952.5 eV, corresponding to Cu^+ $2p_{3/2}$ and Cu^+ $2p_{1/2}$, and those at 933.8 and 954.1 eV were assigned to Cu^{2+} $2p_{3/2}$ and Cu^{2+} $2p_{1/2}$, including the satellite peaks at 941.8 and 961.7 eV.³⁹ Similarly, in the Co 2p XPS spectrum, peaks at 780.5 and 796.8 eV reflect $\text{Co}^{2+} \ 2p_{3/2}^{3}$ and $\text{Co}^{2+} \ 2p1/2$, and the 777.8 and 793.3 eV peaks correspond to $\text{Co}^{3+} \ 2p_{3/2}$ and $\text{Co}^{3+} \ 2p_{1/2}$, respectively.⁴⁰ The satellite peaks of Co 2p were detected at 787 and 803 eV. The satellite peaks observed can be explained as due to the overlapping of antibonding orbitals between Cu, Co, and Se, as has been reported previously. ³⁷ The XPS peaks corresponding to the Se 3d states were observed at 54.1 and 55 eV, corresponding to Se $3d_{5/2}$ and Se $3d_{3/2}$, respectively, demonstrating the existence of Se^{2-.37} The peak at 59.2 eV shows the existence of a minute amount of SeO_x species on the surface which can occur due to the surface oxidation of pristine selenide. However, it must be noted that there was no transitionmetal oxide (i.e., Cu-O or Co-O) detected on the catalyst surface. The relative percentages of the various cations present in the composition were estimated as 9% Co³⁺, 44% Co²⁺, 8.5% Cu⁺, and 38.5% Cu²⁺, totaling to 100%. It must be noted that the ratio of the total metal (Cu + Co) to Se atomic percentage was obtained close to 3:4. ((15.2 + 25.9): 58.9).

Electrocatalytic Performance for CO₂RR. The CO₂ electrochemical reduction activity of CuCo₂Se₄ was investigated through linear sweep voltammetry (LSV) at a scan speed of 10 mV s⁻¹ in Ar- and CO₂-saturated 0.3 M NaHCO₃ electrolyte solution. Electrochemical experiments were performed in a two-compartment H-cell where both the catholyte and anolyte were 0.3 M NaHCO₃ solution. In keeping with modern techniques,

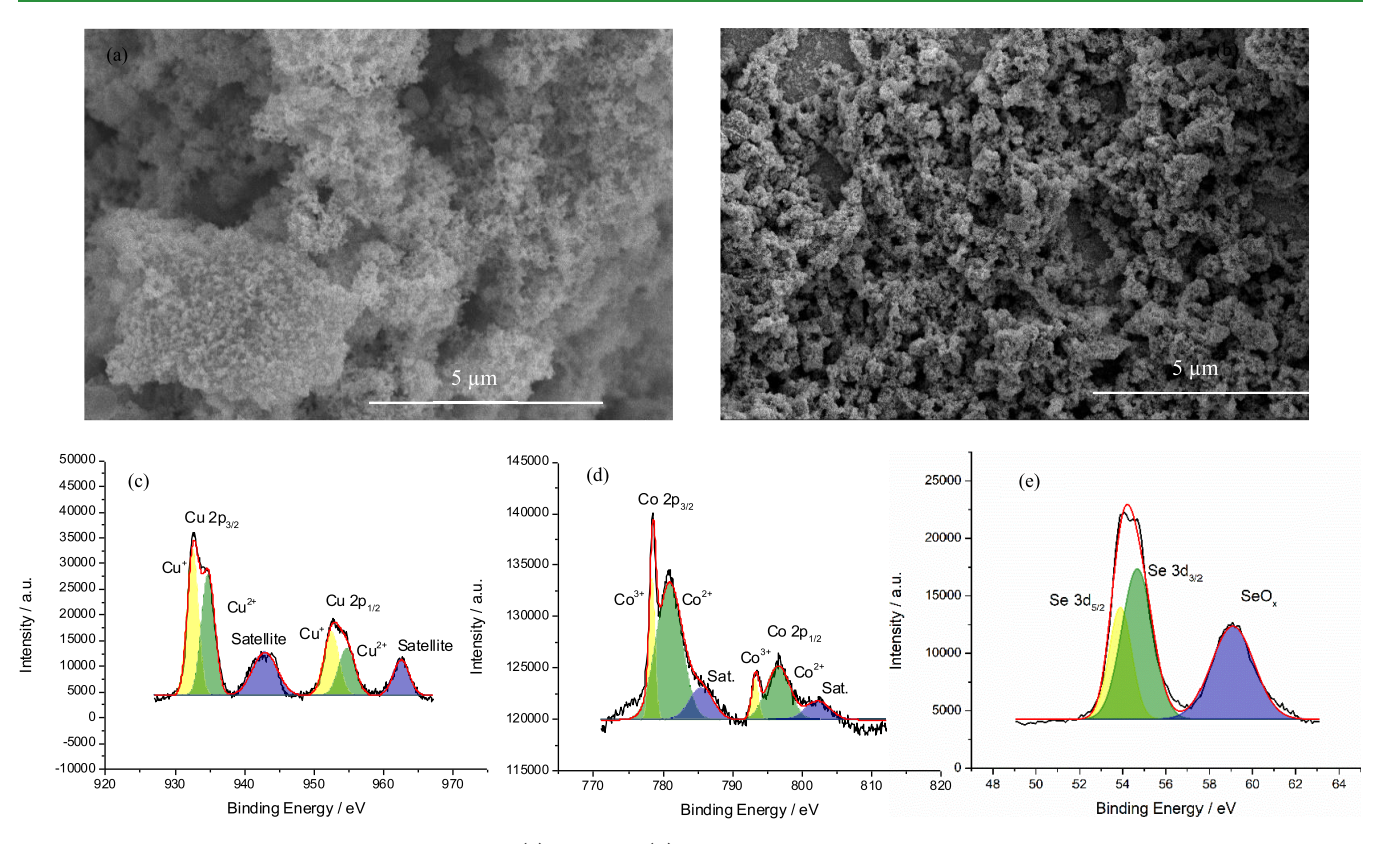


Figure 2. SEM images of CuCo₂Se₄ nanoparticles at (a) high and (b) low magnifications, showing the formation of nanostructures and surface roughness, respectively. (c) Cu 2p, (d) Co 2p, and (e) Se 3d XPS spectra of as-synthesized CuCo₂Se₄.

carbon rod was used as the counter electrode instead of Pt, to minimize impurity enrichment in the electrolyte. Using a Pt wire in $\rm H_2$ -saturated $\rm H_2SO_4$ solution, the AglAgCl reference electrode was standardized utilizing an open-circuit potential (OCP, 0.199 V). All the reduction potentials measured with the AglAgCl reference electrode were converted to RHE using eq 1, and the reported current densities were calculated, taking the geometric area of the electrode into consideration.

$$E_{\text{RHE}} = E_{\text{Ag|AgCl}} + 0.059 \text{pH} + E^{0}_{\text{Ag|AgCl}}$$
 (1)

where $E_{\rm RHE}$ = converted potential vs RHE, $E_{\rm AglAgCl}$ = experimentally obtained potential, $E_{\rm AglAgCl}^0$ = standard potential of AglAgCl (0.199 V).

It must be mentioned here that, in order to be compliant with the standard protocol of data collection and reporting,⁴¹ our electrochemical setup for CO2RR was calibrated by measuring the electrocatalytic activity of polycrystalline Ag electrode and comparing the results with previous reports. The polycrystalline Ag electrode showed no product formation at -0.25 V, while CO, H₂, and formate were identified at -0.9 V, as shown in Figure S1 (Supporting Information), which matches with the previous reports for Ag electrode. These results confirmed the reliability of our electrochemical setup. The CuCo₂Se₄-modified electrode, on the other hand, showed the formation of acetic acid at 0.25 V, and methanol, ethanol, acetic, and formic acid at -0.9 V, confirming the superior performance compared to Ag. The CO2RR current density obtained with the Ag electrode in our electrochemical setup also matched with the previous report, 42 providing further confirmation regarding the reliability of these electrochemical measurements.

The LSV plots were measured in a stirred solution under continuous purging of CO₂ to minimize mass-transfer

limitations. The control experiment (without CO₂) involved purging with Ar under similar conditions. The LSV plots of CuCo₂Se₄-modified electrodes were compared with that of a bare carbon cloth measured under similar conditions to confirm the catalytic effect of CuCo₂Se₄ for CO2RR. CuCo₂Se₄@CFP showed an increased reduction current when a CO₂-purged electrolyte was used compared to Ar-purged electrolyte ash, as shown in Figure 3a, which confirmed that CuCo₂Se₄@CFP was indeed more active toward CO2RR and suppressed the competing HER under these conditions. Bare CFP, on the other hand, did not show any significant activity toward CO2RR, which confirmed the catalytic activity of CuCo₂Se₄ and no substrate effect. The CuCo₂Se₄ catalyst also exhibited a high current density, reaching up to 26 mA cm⁻² at a low applied potential of 800 mV.

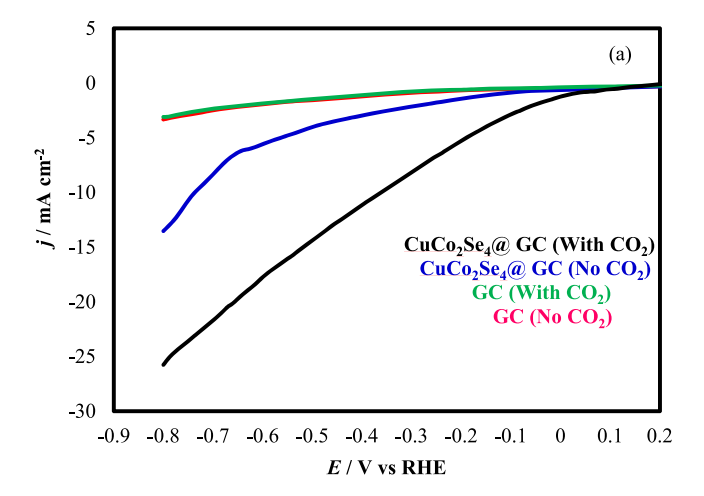
The Tafel slopes of the catalyst were estimated to explore the chemical kinetics of CO₂ electrochemical reduction.

The Tafel slope can be calculated using eq 2:

$$\eta = \alpha + (2.3RT)\log j/\alpha nF \tag{2}$$

where η = overpotential, α = transfer coefficient, n = number of electrons involved in the reaction, F = Faraday constant, j = current density, and slope = $2.3RT/\alpha nF$.

The Tafel slope was determined in the kinetically controlled area of CO2RR under a scan speed of 10 mV s⁻¹. It was observed that the CuCo₂Se₄@CFP electrode exhibited the lowest value of Tafel slope with a value of 237 mV dec⁻¹ in the CO₂-purged electrolyte, as shown in Figure 3b. Typically, the initial single-electron transfer step for the adsorbed radical intermediate (CO₂⁻⁻) formation has a theoretical Tafel slope of 118 mV dec⁻¹. A similarly high Tafel slope for this catalyst suggests that the mechanism of CO2RR over CuCo₂Se₄@CFP may involve a



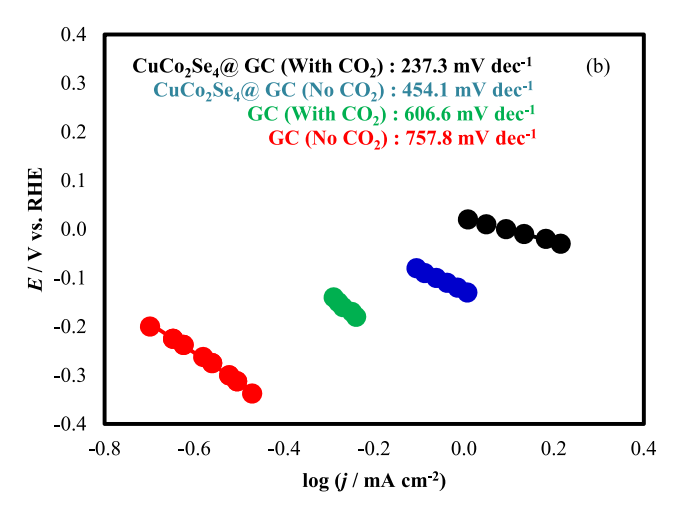


Figure 3. (a) LSVs measured in 0.3 M NaHCO₃ at a scan rate of 10 mV s⁻¹ in the presence and absence of CO₂ with different electrodes. (b) Tafel plots measured in 0.3 M NaHCO₃.

similar electron transfer step and the formation of a radical anion as the chemical rate-determining step (RDS). A much lower Tafel slope closer to 59 mV dec $^{-1}$, on the other hand, indicates a rapid one-electron transfer step, followed by the formation of formate as the RDS. 43 Moreover, the Tafel slope of bare CFP was higher than that of CuCo_2Se_4 , indicating that electron transfer at the CuCo_2Se_4 @CFP electrode surface was much faster.

Chronoamperometry studies were used for detecting and quantifying the product composition generated by the electrochemical reduction of CO_2 at different applied potentials from -0.9 to -0.1 V versus RHE for the time period of 1 h. Initially, these electrochemical experiments were started after purging CO_2 vigorously for 30 min. The electrolyte (0.3 M NaHCO₃ aqueous) was then constantly purged with CO_2 at a rate of 20 sccm during the chronoamperometry studies.

The quantification of liquid and gaseous products was done using NMR and GC-TCD. Typically, 0.1 μ L of DMSO was used as an internal standard mixed with 500 μ L of aliquot (reaction solution) and 100 μ L of D₂O for conducting NMR studies. Water suppression technique was used to suppress the water peaks in the NMR spectra. The detailed calculation for various product yields at different applied potentials and the corresponding faradaic efficiency are shown in the Supporting Information. Gaseous products were detected and quantified

using the GC-TCD technique and using the calibration curves of standards.

It was observed that the composition and selectivity of CO2RR products at the CuCo₂Se₄@CFP electrode varied with the applied potential, as shown in Figure 4a. Specifically, at lower

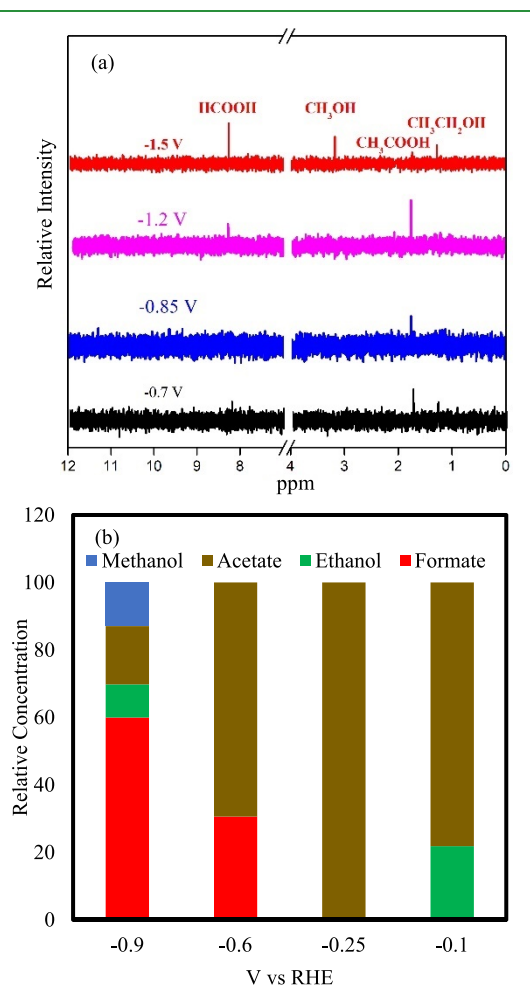


Figure 4. (a) NMR spectra identifying CO_2 reduction products in reaction aliquots collected at different potentials. (b) Plots illustrating the relative concentrations of liquid products quantified from NMR at different stationary applied potentials.

negative potentials, C2 products such as ethanol and acetate were obtained preferentially, while C1 products formed at high negative potentials. Acetate was the major product formed till -0.6 V versus RHE. This is drastically different from other Cu-and non-Cu-based catalyst systems known for CO2RR which produce formic acid and other C1 products at these potentials. Also, such high selectivity indicates a high production rate due to the fact that all the energy is getting used to form the C2 products.

The advent of formic acid in the product composition was observed at -0.6~V (vs RHE) in addition to carbon-rich C2 products. Previously, it was reported that rapid hydrogen production with a decreasing potential results in a decreasing pH near the electrode surface due to continuous hydrogen evolution. Such reduced pH and high concentration of hydrogen lead to the spontaneous conversion of CO_2 to HCO_3^- in situ, leading to the facile formation of formic acid at a higher applied potential.

The relative product yield was calculated by quantifying the products at different potentials using standard calculations, as has been reported previously. ⁴⁴ Figure 4b shows the product selectivity achieved at various applied potentials. A lower applied potential favors the formation of C2 products (acetic acid and ethanol) exclusively rather than C1 products (formic acid) which form in smaller quantities at a higher negative potential. These results illustrate the potential of this catalyst for industrial applications, as the energy input is less and selectivity is high for specific products.

GC-TCD was used for the characterization and quantification of the gaseous products. The head-space gas was collected after 1 h of CO2RR at different applied potentials (-0.1, -0.25, -0.6, and -0.9 V vs RHE), wherein hydrogen was detected with FE = 0, 0.51, 0.90, and 2.7%, respectively, as shown in Figure 5 and

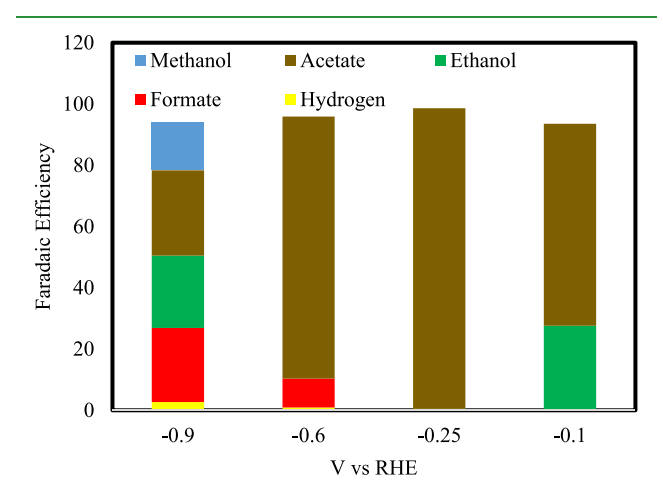


Figure 5. Bar plots depicting the relative faradaic efficiency of cumulative liquid- and gas-phase CO₂ reduction products at different applied potentials quantified through NMR and GC-TCD.

Tables S1–S4. It should be noted that no other hydrocarbon gas or CO was observed during these measurements. Hydrogen evolution is a competing reaction which restricts the faradaic efficiency of hydrocarbon products. The LSV plot of the experiment done on CuCo_2Se_4 @CFP in an Ar-purged electrolyte also suggests that HER becomes more prominent at higher negative potentials, as shown in Figure 3a. Hydrogen formation during CO2RR can be observed starting at -0.6~V versus RHE. Interestingly, no CO was detected in the head-space gas at any applied potential. Such an absence of CO in the product composition yields further confirmation that the preferential formation of C2 products follows a longer dwell time and further reduction of adsorbed intermediate *CO on the catalyst surface inhibiting its ready desorption.

It must be mentioned here that the choice of the carbonate electrolyte and its apparent effect on CO2RR activity have also been researched previously. Apart from NaHCO₃, potassium bicarbonate (KHCO₃) has also been commonly used as an electrolyte. Hence, to be compatible with other CO2RR reports, these experiments were also conducted in KHCO₃ electrolyte. Interestingly, it was observed that the product composition does not change drastically over the applied potential range, as shown in Figure S2 (Supporting Information), and the formation of the C1/C2 products along with their relative distribution follows the same trend as that for the NaHCO₃ electrolyte. Various studies reported previously have suggested that NaHCO₃ is a better electrolyte than KHCO₃ due to the improved charge

transfer at the electrode interface. A detailed discussion of the various bicarbonate electrolytes compiled from previous reports has been included in the Supporting Information. Overall, the rate of electrocatalytic CO_2 reduction is affected by improved mass transport, irrespective of the electrode geometry and electrolyte. However, to be consistent with the investigation of other $\mathrm{CO}_2\mathrm{RR}$ electrocatalysts, we have focused on NaHCO_3 electrolyte in this study.

We have investigated the formation rates and ECSAnormalized partial current density for every product over a series of potentials to gain a better understanding of the specificity of the CO₂ reduction reaction and to comprehend the reaction dynamics. This type of examination for various products can yield critical mechanistic insights. The analyses of reaction rates (Figure 6a) and ECSA-normalized partial current density (Figure 6b) revealed that acetic acid was the most important factor in increasing activity throughout a broad range of applied potentials. Formic acid formed at a level

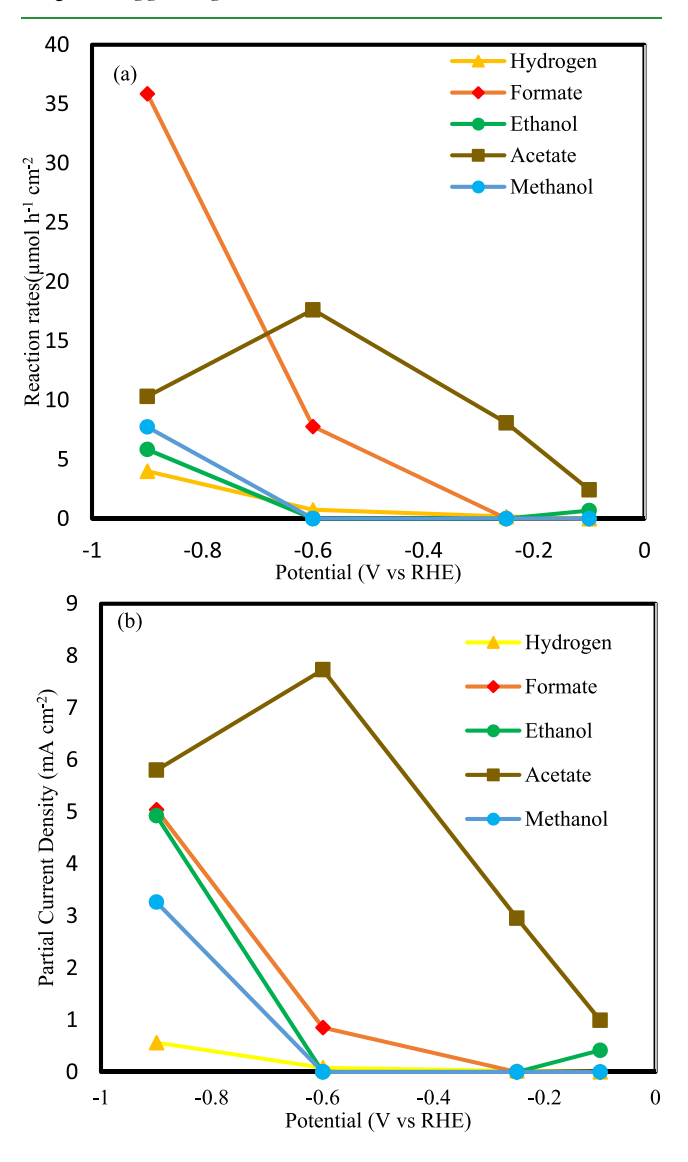


Figure 6. CO₂RR performances of CuCo₂Se₄ catalyst. (a) Reaction rates for formation of hydrogen, formate, ethanol, acetate, and methanol. (b) ECSA-normalized partial current density for formation of individual products: hydrogen, formate, ethanol, acetate, and methanol.

proportional to acetic acid at a higher applied voltage. Acetic acid and ethanol, on the other hand, formed at significantly larger rates when the applied potential was low. The turnover number (TON) for different products at each applied potential was also estimated, as shown in Figure S3 in Supporting Information. The TON of formic acid was observed to be maximum at -0.9 V, while acetic acid showed higher TON at -0.6 V at lower applied potentials. These performance patterns validated the catalyst's product selectivity (toward C2 products) and novelty when compared to conventional CO2RR catalysts that have greater formation constants for primary C1 products. Such a difference in electrochemical activity can be attributed to the different rates of intermediate *CO conversion on the catalyst surface, as described below. Dehydroxylation and decarbonylation of chemical intermediates can also occur at varying rates depending on the applied voltage. Such findings also show that CuCo₂Se₄ is catalytically active for CO₂ reduction and generates considerable amounts of carbon-rich compounds at high rates over longer durations.

Intrinsic characteristics such as rapid catalyst activation via intermediate adsorption and improved charge transfer are often attributed to increased catalytic performance. On the other hand, electrolyte and analyte exposure to the active sites is influenced by extrinsic variables like morphology of the catalytic grains and surface roughness. External parameters influencing electrocatalytic activity were estimated using a previously described experimental technique. Hy measuring the double-layer capacitance within the non-Faradaic zone as a variable of scan speed and comparing the specific capacitance (*C*) to the double-layer capacitance measured, electrochemically active surface area was calculated.

The electrochemical double-layer capacitance ($C_{\rm DL}$) was calculated following eq 3

$$i_{\rm DL} = C_{\rm DL} \times \nu \tag{3}$$

where $i_{\rm DL}$ represents the current observed, while ν is the scan rate. As can be seen from Figure 7, $C_{\rm DL}$ calculated from the i versus ν plot resulted in a value of 0.02 mF.

The ratio of $C_{\rm DL}$ and $C_{\rm S}$ was used to calculate ECSA, as shown in eq 4.

$$ECSA = C_{DL}/Cs \tag{4}$$

The cyclic voltammograms were recorded at scan speeds ranging between 5 mV/s and 200 mV/s in CO₂-purged 0.3 M NaHCO₃. Polarization curves were measured in the potential range of 15 mV according to OCP of the CuCo₂Se₄ electrode. Current density was displayed as a function of scan rate using cyclic voltammograms.

The capacitance values were used to derive the surface roughness factor. The ECSA ratio was derived from Cs obtained from the reported data $(40~\mu F~cm^{-2})^{45}$ and $C_{\rm DL}$ from the plot (0.071~mF). The ECSA value was calculated to be $1.76~cm^2$. The effect of catalyst morphology on the working electrode was also estimated from the roughness factor (RF). RF was calculated to be 6.24~from the ratio between ECSA and the geometric electrode area $(0.283~cm^2)$. The high value of ECSA and the roughness factor depict that CO_2 dissolved in the electrolyte has more access to the catalytic sites on the working electrode, leading to a better conversion efficiency.

For further investigation of the electrochemical performance of CuCo₂Se₄@CFP toward CO2RR, EIS (electrochemical impedance spectroscopy) was performed, as shown in Figure 8. The internal resistance of the catalyst composite and the

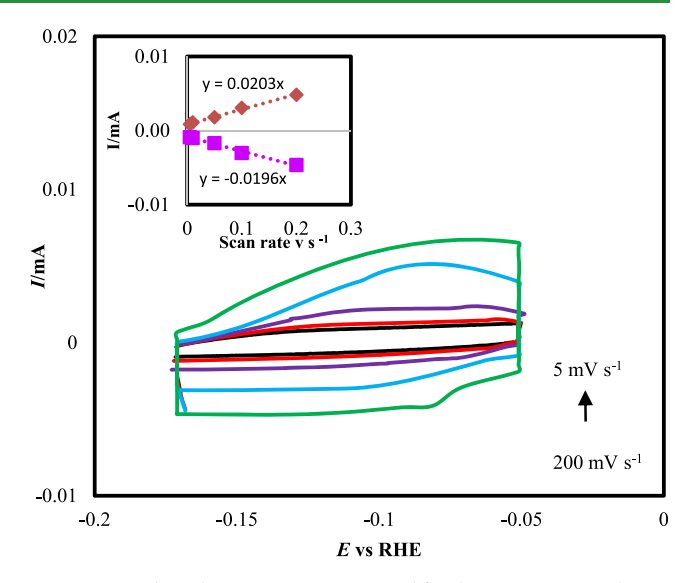


Figure 7. Cyclic voltammograms measured for the $CuCo_2Se_4$ catalyst in 0.3 M NaHCO₃ under continuous Ar purging at different scan rates from 5 to 200 mV s⁻¹ for the determination of ECSA. Inset shows the plots of anodic and cathodic currents measured at -0.12 V vs RHE as a function of scan rate.

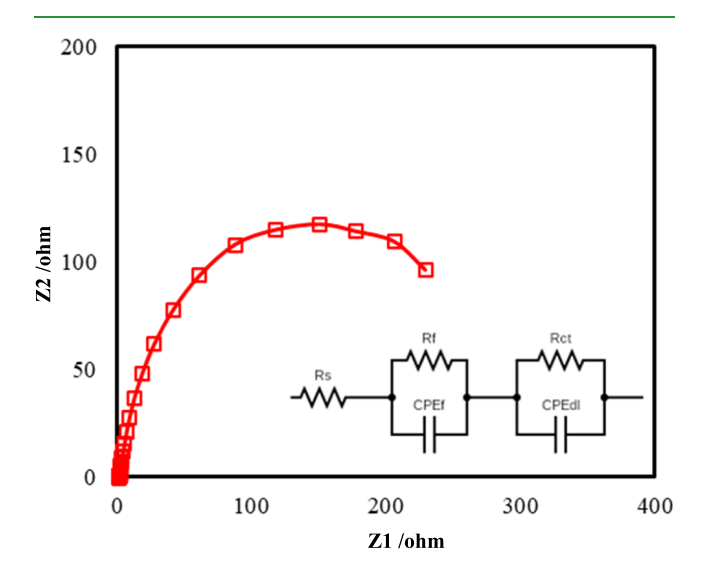


Figure 8. EIS Nyquist plots of CuCo₂Se₄@CFP in CO₂-saturated 0.3 M NaHCO₃ electrolyte (pH 6.8) from 0 V to -1.3 V vs RHE. Inset shows the equivalent circuit fitted to the experimental spectra, where $R_{\rm ct}$ corresponds to the charge-transfer resistance on the catalyst–electrolyte interface, while $R_{\rm s}$ indicates the film resistance of the catalyst composite.

charge-transfer resistance at the (electrode)—electrolyte interface of the catalyst were calculated by performing EIS and analyzing the Nyquist plots measured in CO₂-saturated 0.3 M NaHCO₃ under an applied potential of 0.1 V versus RHE. This plot was fitted with the equivalent circuit and electrolyte resistance ($R_{\rm s}$), resistance of the catalytic composite ($R_{\rm f}$), and charge-transfer resistance ($R_{\rm ct}$) estimated from the circuit. The uncompensated electrolyte resistance values, $R_{\rm s}$, $R_{\rm ct}$ and $R_{\rm f}$ of the catalyst composite were 1.69, 40, and 230 Ω , respectively, as obtained from the fitting of the equivalent circuit, and shown in Table 1.

The charge-transfer resistance, $R_{\rm ct}$, which is estimated from the lower frequency region illustrates the charge transferability of the CO2RR process occurring on the catalyst surface. A lower

Table 1. Fitting Parameters Obtained from Nyquist Plots at Various Potentials

resistor and capacitance	value
$R_{ m s}/\Omega$	1.69
$R_{ m f}/\Omega$	230
$R_{ m ct}/\Omega$	40
CPEdl/F	0.002
CPEf/F	0.0023

 $R_{\rm ct}$ value indicates an efficient and fast electron transfer at the catalyst–electrolyte interface, resulting in a faster CO₂ reduction rate, better catalytic activity, and lower overpotential, which can be seen from the electrocatalytic measurements mentioned above. $R_{\rm f}$ on the other hand, influences the charge transport within the catalyst composite. Hence, lower $R_{\rm f}$ can result in high current density and faster kinetics at low applied potentials.

Electrochemical Performance of CuCo₂Se₄ for Alcohol Oxidation Reaction. The electrocatalytic performance of CuCo₂Se₄ toward complementary alcohol electro-oxidation was also investigated using a three-electrode H-cell setup. LSV polarization curves measured in the absence and presence of 1 mol L⁻¹ methanol and ethanol in 1 M KOH showed that CuCo₂Se₄ was active for anodic alcohol oxidation reaction (AOR). The results from LSV demonstrate a moderate level of AOR activity, with an anodic current density of 75 mA cm⁻² at the potential of 1.45 V versus RHE, as shown in Figure 9a. When methanol was added to make a solution of 1 M methanol, the polarization curve recorded showed enhanced activity. Also, it was observed from the polarization curves that the overpotentials changed by 250 and 300 mV at 15 and 50 mA cm⁻²,

respectively, when compared to water-splitting potentials. When ethanol was added, the overpotentials got reduced by 230 mV and 260 mV at 15 and 50 mA cm⁻², respectively. This implies that for industrial applications in alcohol-based fuel cells, very less cell potential needs to be applied, and at that cell potential, CO2RR-AOR will produce the same product in both the compartments of H-cell. The Tafel slopes calculated from the polarization curves offered more insights into the underlying kinetics as explained below.

The Tafel slope was lower in the case of methanol and ethanol oxidation, exhibiting values of 78.6 and 52.7 mV dec⁻¹, respectively, when compared to water splitting, as shown in Figure 9b. This indicates that the kinetics improve when methanol and ethanol are present in the anolyte solution. Also, it proves that mass transfer is enhanced, and a larger number of catalytic sites present in the electrode surface are available. For the identification of the products of alcohol oxidation in the anodic compartment, ¹H NMR was used. Formic acid was detected at the chemical shift of 8.3 ppm in the anodic compartment when methanol was added, and acetic acid was observed at the chemical shift of 1.7 ppm when ethanol was added (Figure 9c,d) in the anolyte. The stability of the CuCo₂Se₄ electrode under cathodic and anodic potentials was confirmed through XPS measurements performed after CO2RR and alcohol oxidation. These postcatalytic activity XPS measurements showed no changes of the Cu, Co, and Se XPS peaks compared with those of the pristine catalyst, as shown in Figure S4 in Supporting Information. This confirms that the CuCo₂Se₄ surface is indeed stable under the conditions of CO2RR and alcohol oxidation at potentials as mentioned above.

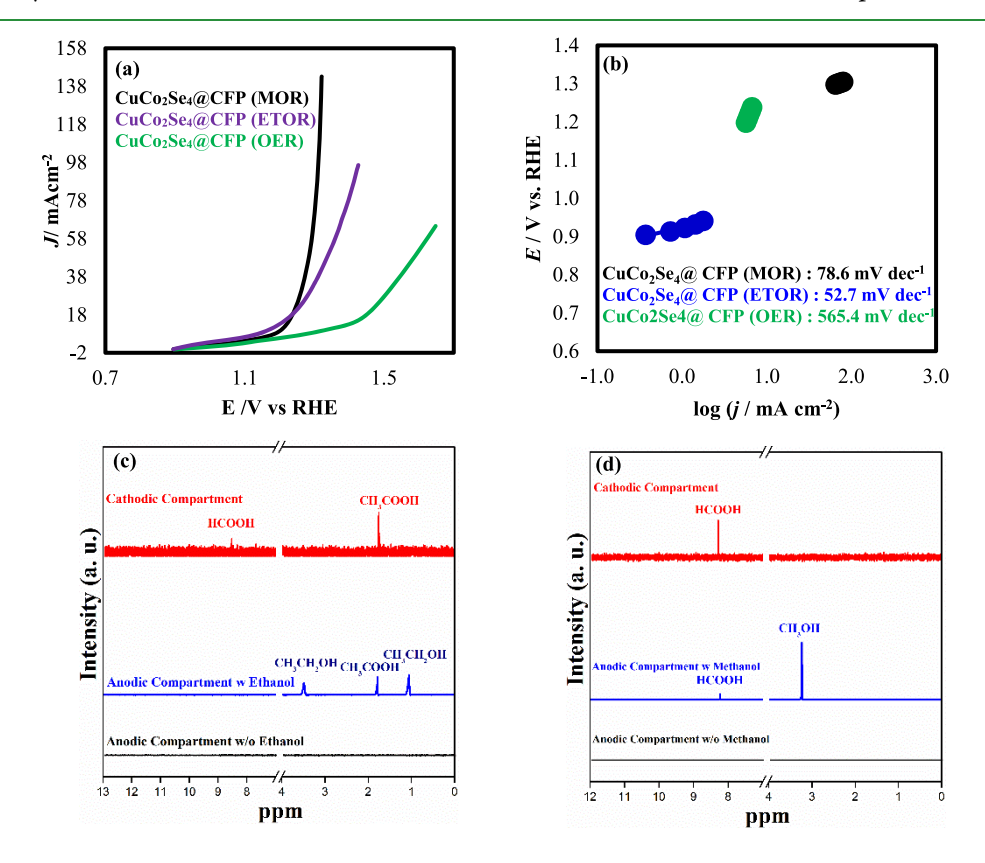


Figure 9. Electrocatalytic performances of $CuCo_2Se_4/CFP$. (a) The polarization curves of $CuCo_2Se_4/CFP$ in the absence (green) and presence of 1 M ethanol (purple); 1 M methanol (black) in 1 M KOH solution. (b) Tafel plots of the above polarization curves. (c) ¹H NMR spectra of the anodic and cathodic compartments of ethanol oxidation (EOR). (d) ¹H NMR of the anodic and cathodic compartments of methanol oxidation (MOR).

It must also be mentioned that previously CuCo₂Se₄ was also reported for OER activity at a much higher anodic potential, wherein it showed similar stability.

Long-term chronoamperometry experiments were also conducted at a fixed potential of 1.5 V versus RHE to detect the rate of methanol oxidation and to determine the rate of formic acid production. The rate of reaction stagnates over time which can be revitalized by adding more methanol, hence improving the mass-transfer kinetics. The current density of CuCo_2Se_4 goes through little change over a long period (100 h), as shown in Figure S5 in Supporting Information, signifying its applicability to the industry.

Electrochemical Catalytic Activity of CuCo2Se4 for CO2RR-AOR Combined Reaction (CuCo2Se4/CFIICu-Co₂Se₄/CF). Because of the enhanced activity of the catalyst for CO2RR in the cathodic compartment and alcohol oxidation in the anodic compartment, a two-electrode H-cell was set up with a CuCo₂Se₄ catalyst-loaded working electrode as an anode having 1 M CH₃OH or 1 M C₂H₅OH along with 1 M KOH in the electrolyte and a CuCo₂Se₄ catalyst loaded on the counter electrode as the cathode in 0.3 M NaHCO3 solution. This electrolyzer operated at ambient temperature and pressure, producing the same product in both compartments. The polarization curves from linear scan voltammetry showed that a standard current density of 15 mA cm⁻² was obtained in CO2RR-methanol oxidation and CO2RR-ethanol oxidation at cell potentials of 0.67 and 0.73 V, respectively. Most importantly, these cell potentials are 280 and 220 mV less than what is required when no alcohol is added under the same setup. The voltages were found to be significantly smaller than the theoretical voltage [1.299 V in eq 1] for the overall CO2RR (no alcohol present). When methanol was a reactant in the anodic compartment, formic acid is produced in the electrolyzer at a potential of 0.7 V. When ethanol was present in the anodic chamber, acetic acid was produced at 0.75 V. It must be noted that there was no leaching of hydrocarbon species between the cathodic and anodic chambers through the Nafion membrane, as confirmed by collecting NMR spectra from the analyte under active potential which showed the presence of no hydrocarbons in the absence of methanol/ethanol (black line plots in Figure

Also, 50 mA cm^{-2} current densities were obtained at 0.77 and 0.78 V for methanol and ethanol oxidation, respectively. The faraday efficiency obtained for acetate production in the anodic and cathodic compartments was 71.35 and 92.20%, respectively, at an overall cell potential of 0.7 V. For formate production, FE was 84.35 and 92.50% in the anodic and cathodic compartments, respectively, at the cell voltage of 0.75 V.

DFT Calculation on Catalyst Surfaces: Estimation of CO Adsorption Energy and Surface Band Structure. The CO adsorption on the (100) $CuCo_2Se_4$ surface was investigated further using density functional theory (DFT) electronic band structure calculations within magnetic GGA + U approximation, as shown in Figures 10 and 11. Recent DFT calculations for bulk and slab $CuCo_2Se_4$ have shown that hybridization of Se p states with Cu and Co d states constitutes the valence band, whereas the vacant d states of Co and antibonding p states of Se form the conduction band. These observations suggest a possibility of d—d electron transfer between Co and Cu along with the metalto-anion (Se) charge transfer. Also, the continuity of DOS in the vicinity of the Fermi level suggests that $CuCo_2Se_4$ has enhanced conductivity, which is also evident from the EIS data that show a low resistance (R_{ct}) of bulk $CuCo_2Se_4$. A comparison of the

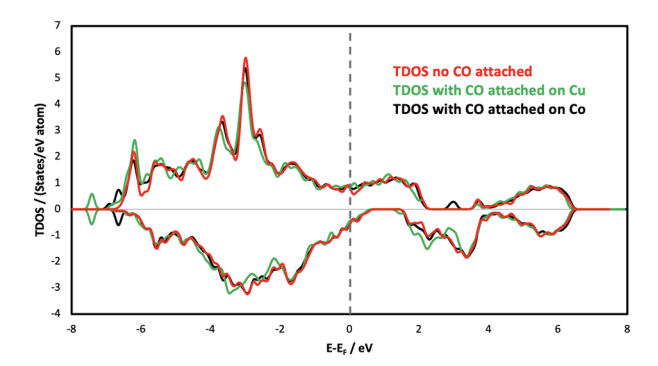


Figure 10. Spin-resolved total density of states (TDOS) for a CuCo_2Se_4 (100) slab with and without CO attachment on either Co or Cu sites at the surface layer.

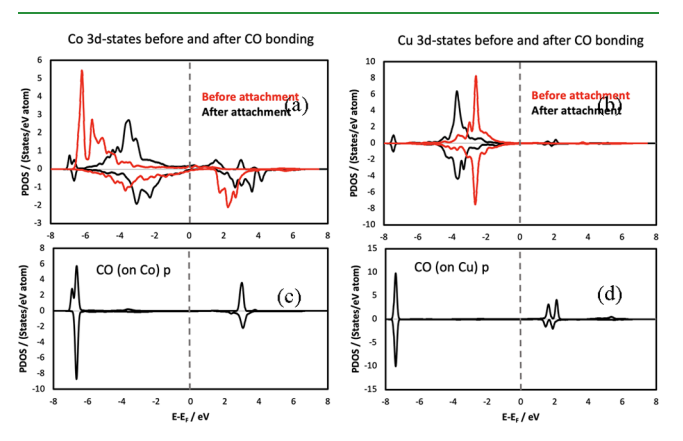


Figure 11. Spin-resolved partial density of states (PDOS) for the metal 3d states before and after CO attachment on either (a) Co or (b) Cu sites at the surface layer. The partial DOS for CO p-states is also shown in (c) and (d).

results of GGA (U = 0) and GGA + U calculations suggested that the on-site Coulomb interactions are required for obtaining the magnetic solution. We also performed hybrid Heyd–Scuseria–Ernzerhof (HSE06) calculations with a mixing parameter of 0.25 and a screening parameter α of 0.2 Å⁻¹ and a cut-off energy of 500 eV. The self-consistent HSE06 calculations for the Cu₁₄Co₂₈Se₅₆ surface structure that included spin and set the initial magnetic moments to 2.0 μ B for all Co atoms converged to a nonmagnetic solution with magnetic moments on Co of 0.0–0.3 μ B, which is significantly lower than that of GGA + U values of 0.8–2.0 μ B. Therefore, we conclude that the GGA + U approach is required in order to obtain the magnetic solution, as should be expected for Co-containing material.

To calculate the CO adsorption energies, first, the total energy of a clean relaxed surface ($E_{\rm clean}$) was calculated; then, a single CO molecule was attached over the Co or Cu sites at the initial distance of ~1.80 Å taken from the bond lengths of metal carbonyl complexes. Upon optimization, the total energy of the surfaces, with CO bonded to either Co or Cu surface atoms, was calculated ($E_{\rm sys}$). The adsorption energy of CO on the (100) surface was found according to the equation: $E_{\rm ad} = E_{\rm sys} - E_{\rm clean} - E_{\rm CO}$, with $E_{\rm CO}$ being the energy of a free CO molecule. The optimized atomic structures for the (100) surface of CuCo₂Se₄, with CO bonded to either Co or Cu along with the calculated spin-resolved charge transfers, are shown in Figure 12.

First, to establish which metal atom on the surface is more likely to be the catalytically active site for CO2RR, the

ı

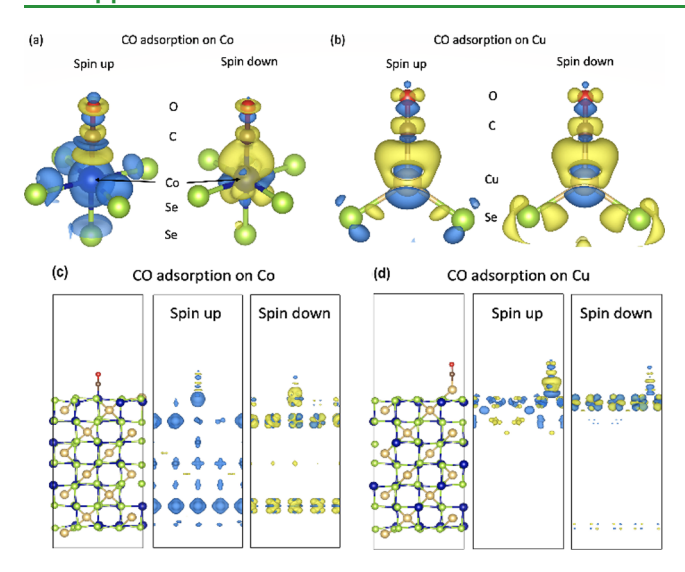


Figure 12. Optimized atomic structures for the (100) surface of $CuCo_2Se_4$, with CO bonded to either Co or Cu along with the total charge density distribution throughout the slabs. The spin-resolved charge density maps in the nearest neighbor shell after CO adsorption on (a) CO and (b) Cu. (c) and (d) Charge density distribution over the entire slab.

adsorption of CO on (100) Co/Cu-terminated slabs was modeled by placing a single CO molecule directly above the active metal site (Co or Cu) of the relaxed unpassivated surface at the initial metal-C distance of about 2.2 Å and then fully optimizing the structure. The GGA (U = 0) approach predicts that CO adsorption on the surface Cu atom ($E_{ad} = -0.92 \text{ eV}$) is 0.45 eV higher as compared to that on Co ($E_{ad} = -1.37$ eV). However, when the on-site Coulomb interactions are taken into account and the magnetic solution is attained, the opposite trend emerges: the energy of CO absorption on the surface Cu atom $(E_{\rm ad} = -1.53 \text{ eV})$ is lower than that on the Co atom $(E_{\rm ad} = -0.91 \text{ eV})$ eV). The large energy difference of 620 meV suggests that Cu atom is the highly preferred catalytically active site, although CO attachment to Co is also likely, given the negative adsorption energy. It should be noted that an OH adsorption on the (100) surface of CuCo₂Se₄ that showed a preference for Co atom in GGA + U calculations was accompanied by an increased magnetic moment on Co upon its bonding with OH.³⁴ Therefore, it is important to understand the microscopic mechanisms of CO adsorption and its effects on the electronic and magnetic properties of the metal states at the surface.

Upon bonding to the CO complex, the optimized Cu-Se and Co-Se distances, on average, increase from 2.24 to 2.37 Å and from 2.33 to 2.45 Å, respectively. Consistent with the weaker metal−Se interactions, the metal−C bonding weakens the C≡ O bond to a partial double-bond character, as evident from the longer optimized C-O distance, found to be equal to 1.15 Å and 1.16 Å for CO adsorption on Cu and Co, respectively, as compared to 1.14 Å for a free-standing CO molecule, calculated using the same methods. The Co(Cu)-CO distance is 1.75 Å (1.83 Å), whereas the Co(Cu)-C-O angle is 178.9° (179.5°). Most importantly, it is found that the CO adsorption affects both the magnetic interactions on the Co atom that bonds to CO as well as the magnetic moments of other Co atoms in the slab for CO attachment to nonmagnetic Cu. The changes in the magnetic moment of Co atoms in various layers after the attachment of CO on the CuCo₂Se₄ surface have been listed in Table 2. Specifically, the local magnetic moment on the Co atom

Table 2. Magnetic Moments on Co Atoms in each Layer of the (100) Slab, as Estimated from GGA + U DFT Calculations. Each Layer has Four Co Atoms, and Four Values Are Shown for the Layers in which the Co Magnetic Moments Differ. Otherwise, an Average Value Is Given

	magnetic moment on Co atoms, $\mu_{\rm B}$		
$CuCo_2Se_4$ (100) slab	CO- free	CO adsorption on Co	CO adsorption on Cu
top layer 1	2.1	1.1, 2.2, 2.1, 2.0	2.1
layer 2	0.9	2.0, 2.1, 1.0, 0.9	0.9
layer 3	0.9	0.9	0.9
middle layer 4	0.8	0.8	2.1
layer 5	0.8	0.9	0.9
layer 6	0.9	0.9	0.9
bottom layer 7	2.1	2.1	2.1

decreases from 2.0 $\mu_{\rm B}$ to 1.1 $\mu_{\rm B}$ upon bonding with CO. This observation is in contrast to our previous studies where the -OH adsorption on Co increases the magnetic interactions on Co.³⁴ The calculated partial DOS, as illustrated Figure 11a, shows that the occupied spin-up and spin-down Co states shift toward positive energy and become more alike and less split upon bonding with CO due to the weaker Co-Se interactions and weaker magnetic exchange splitting. At the same time, the magnetic moments of the two nearest Co neighbors located in the second layer of the slab increase from 0.9 μ_B to 2.0 μ_B . The remaining Co atoms maintain their magnetic moments with respect to those in the CO-free interface. When CO is attached to nonmagnetic Cu, the magnetic moments of the surface Co as well as Co atoms in the second layer remain similar to those in the CO-free surface. However, the magnetic moments of all four Co atoms in the fourth layer in the slab increase from 0.8 $\mu_{\rm B}$ to $2.1 \mu_{\rm B}$. The increase of the magnetic moments for the entire layer as opposed to the magnetic moment redistribution, as seen in case of the adsorption on Co, leads to more pronounced differences in the total DOS for the CO adsorption on Cu and is likely to be the reason for the higher catalytic activity of the Cu site. This suggests that magnetism on the surface and subsurface layers plays a crucial role in favoring the CO adsorption on Cu.

The spin-resolved charge transfer, upon adsorption of CO, was also calculated, as shown in Figure 12. In this calculation, the charge density of the lattice without CO and the charge density of CO are subtracted from the charge density of the relaxed lattice, with CO attached. The difference represents the charge transfer due to Co or Cu bonding with CO. The yellow color means positive density which is the new charge density that appears upon bonding, whereas blue color means negative charge density--the charge density that is transferred away from those areas. Overall, the plot reveals the charge density redistribution from blue areas to yellow. The charge densities are spin-resolved, so that the transfer between d-orbitals with spin up and spin down can be seen. For CO on Co, the charge redistribution is mainly between the spin-up and spin-down dstates of Co, possibly between the metal d-orbitals. Se atoms also lose the charge in the spin-up channel. For CO adsorption on nonmagnetic Cu, the charge transfer on Cu is identical for spin up and spin down, as expected. However, Se states lose charge within the spin-up and gain charge within the spin-down

The latter occurs because of the interaction of Se with the magnetic Co: the surface Co atoms show strong charge transfer between their spin-down orbitals upon CO adsorption on Cu

(Figure 12c,d). A similar orbital cloud redistribution happens for the Co atoms in the second layer in the case of CO adsorption on Co. Interestingly, for the Co-CO case, there is a symmetrical Co charge redistribution for the second layer from the bottom (CO-free) surface. The magnetic moments of those Co atoms are maintained, implying that the charge redistribution does not affect the magnetic splitting. In the Cu–CO case, the increase of the Co magnetic moments in the middle layer (Table 2) is not accompanied by the charge transfer between orbitals. Because the charge transfer occurs only within the two top layers, the surface and subsurface charge redistributions are influenced by the increased magnetic moments of Co in the middle layer. Interestingly, it was also found that the charge distribution on the C-end of CO molecule was significantly enhanced when bonded to the Cu site compared to that on Co (comparing the yellow lobes in Figure 12a,b). This further suggests that while the metal-to-ligand back-bonding is feasible between both Cu-C≡O and Co−C≡O linkages, it is more pronounced for Cu. The metal-to-ligand back-bonding is one of the primary reasons for improved intermediate *CO adsorption and its longer dwell time on the catalyst surface. Hence, this further implies that Cu in the vicinity of magnetically active Co atoms has significantly better activity for the formation of C2 products. This also suggests that transition metals with high d-electron density in the $t_{2\sigma}$ set have extensive metal-to-ligand back-bonding. Such knowledge will be very helpful for further catalyst surface design to yield selective CO₂ reduction products.

The CO adsorption energy on Cu and Co sites in CuCo₂Se₄ was compared with other CO2RR catalysts reported previously to correlate it with the preferential formation of C1/C2 product based on the hypothesis that larger CO adsorption energy led to longer CO dwell time on the surface, leading to the preferential formation of C2+ products. For metal catalysts like Au or Ag, low CO adsorption energy was observed and has been reported to produce CO as the main product. 11 On the other hand, metal catalysts like Pt, Pd, and Ni have shown high CO adsorption energy. However, these catalysts also show a high binding energy for *H, leading to electron consumption that is utilized for hydrogen evolution rather than electrochemical reduction of CO₂ in aqueous medium. With high CO adsorption energy, catalysts can also get poisoned due to surface passivation by the small amounts of CO produced during the continuous electroreduction of CO₂. Cu and Co metals have showed higher CO adsorption energy compared to metals like Au and Ag but lesser than the catalysts like Pt, Pd, and Ni, as shown in Figure 13. 46–49 Co metal catalyst has been reported to produce CO and hydrocarbons like CH₄, 6,13,21,24 while Cu produces a wide range of hydrocarbons which relates to the moderate CO adsorption energy on these metal catalysts. 14,48,50 CuCo₂Se₄ shows slightly higher CO adsorption energy than Co and Cu but lower than the passivation level observed with Pt, Pd, and Ni catalysts, 11,51,52 which favors further reduction of CO adsorbed on the surface to produce carbon-rich products like acetic acid. The correlation of CO adsorption energy with the preferential formation of C2+ products can be very clearly seen in Figure 13, in which the experimentally observed faradaic efficiency for C1 (CO and formic acid) and C2 (ethanol and acetic acid) products has been plotted as a function of estimated CO adsorption energy for various catalysts. It can be clearly seen that the faradaic efficiency for C2+ products reaches the maximum in the midsection, which exhibits a moderate CO adsorption energy. The effect of reducing anion electronegativity and altering delectron density of the catalytic site is also very apparent from

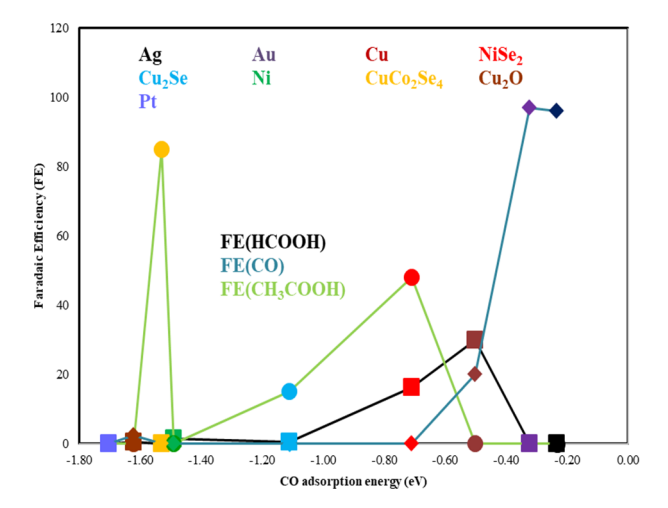


Figure 13. Correlation of CO adsorption energy with faradaic efficiencies of C1 (CO and formic acid) and C2 (acetic acid) product formation for various catalyst surfaces. The line color in the plot indicates specific products, as indicated in the legend, while the symbol colors represent the different catalyst systems, as illustrated in the color key. This figure has been constructed by following CO2RR reports, as found in refs 6, 13, 14, 21, 24, 25, 42, 47–53.

Figure 13, which shows how the same transition element can show a wide variation in CO adsorption energy based on anion coordination and, as the result of this work reveal, on the magnetic interactions of the metal atoms in the vicinity. This can be explained by understanding the mechanism of CO adsorption on the catalyst site. CO adsorption on the catalyst surface proceeds through two possible pathways using coordinate bonds: first is through σ -donation from CO to metal through the highest occupied molecular orbitals (HOMO) located on C and second is through back-donation from the metal (d-orbitals) to CO (π^* , LUMO). The metal-to-ligand back-bonding can be observed from the low-intensity peak near -3.7 eV due to the contribution of CO p-DOS, similar to previously reported results. While a complete theoretical study should involve all of the reaction pathways of the mechanism and explore all the possible lattice planes of CuCo₂Se₄ for understanding the selectivity exhibited by the catalyst toward the formation of specific reduction products, the DFT results in this work prove that the CuCo₂Se₄ catalyst surface facilitates the selectivity toward carbon-rich products by enhancing the intermediate CO adsorption. These DFT results are synchronous with the experimental observations achieved in this study. From the CO adsorption energy calculations on the surface of CuCo₂Se₄, it can also be concluded that Cu atom is the active catalytic site for the CuCo₂Se₄ system. However, the presence of magnetic Co on the neighboring sites influences the electronic density around the Cu ions as well as intermediate adsorption energy.

The novelty of CuCo₂Se₄ as a CO2RR catalyst has been emphasized through a benchmarking figure, as shown in Figure 14. This benchmarking figure compares the performance of various CO2RR catalysts reported by previous researchers with that of CuCo₂Se₄ at different potentials. The performance metric chosen for comparison is the range of products formed, categorizing them as C1/C2 products. As can be seen from the figure, most catalysts predominantly form CO and HCO₂H as the main products, and very few catalysts show high selectivity for the formation of C2+ products. CuCo₂Se₄, on the other hand, shows high selectivity for the formation of acetic acid and ethanol, which highlights the novelty and transformative nature

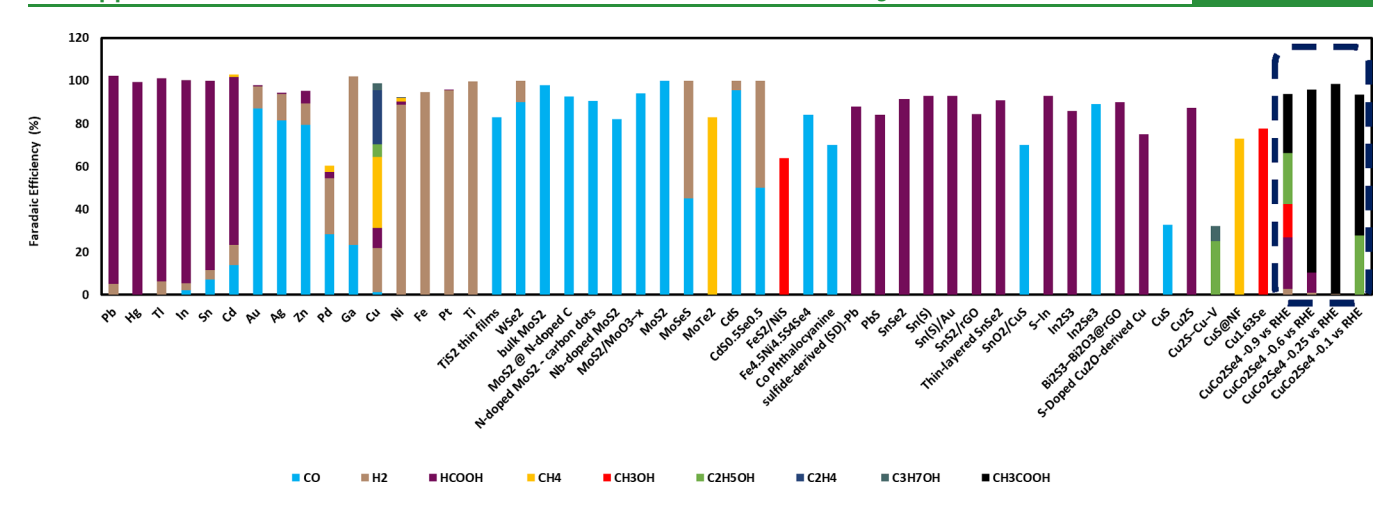


Figure 14. Benchmark figure comparing the CO2RR product distribution of CuCo₂Se₄ with the other reported electrocatalytic systems. The various products formed have been color-coded in the bottom legend.

of this system for CO2RR. The specific references used for creating Figure 14 have been listed in the Supporting Information.

CONCLUSIONS

In this study, CuCo₂Se₄ has been identified as an effective catalyst for the reduction of CO2 to carbon-rich high-value products with high selectivity. The reduction product selectivity has been correlated with intermediate *CO adsorption energy, which confirms that moderate *CO adsorption energy leads to the preferential formation of C2+ products, possibly due to its longer retention and subsequent reduction on the catalyst surface. The CuCo₂Se₄ catalyst produces only acetic acid and ethanol at lower applied potential values, while minor amounts of formic acid are produced at higher applied potentials. As acetic acid and ethanol have higher economical and industrial values, their selective production with low energy expense underlines the novelty of this catalyst. Interestingly, this catalyst is also active for methanol and ethanol oxidation, which further increases its applicability toward addressing the practical challenges for achieving carbon neutrality.

Detailed DFT studies have been performed on the $CuCo_2Se_4$ catalyst surface to estimate the *CO adsorption energies on Cu and Co sites as well as understand the changes in the surface electronic structure as a function of CO adsorption. It was observed that Cu showed more favorable CO adsorption energy compared to Co. More importantly, the presence of the neighboring magnetically active Co atoms significantly influenced the CO adsorption energy on Cu, indicating that the catalyst design plays an even greater role for optimal CO2RR with high selectivity.

ASSOCIATED CONTENT

Supporting Information

The Supporting Information is available free of charge at https://pubs.acs.org/doi/10.1021/acsami.3c00488.

Calibration with Ag electrode for CO2RR, XPS data after CO2RR, details of faradaic efficiency calculation, TON plots, and CO2RR selectivity in potassium bicarbonate electrolyte (PDF)

AUTHOR INFORMATION

Corresponding Author

Manashi Nath — Department of Chemistry, Missouri University of Science & Technology, Rolla, Missouri 65409, United States; orcid.org/0000-0002-5058-5313; Email: nathm@mst.edu

Authors

Apurv Saxena — Department of Chemistry, Missouri University of Science & Technology, Rolla, Missouri 65409, United States Shubhender Kapila — Department of Chemistry, Missouri University of Science & Technology, Rolla, Missouri 65409, United States

Julia E. Medvedeva — Department of Physics, Missouri University of Science & Technology, Rolla, Missouri 65409, United States; o orcid.org/0000-0001-7142-1644

Complete contact information is available at: https://pubs.acs.org/10.1021/acsami.3c00488

Author Contributions

The manuscript was written through contributions of all authors. All authors have given approval to the final version of the manuscript.

Notes

The authors declare no competing financial interest.

ACKNOWLEDGMENTS

The authors would like to acknowledge the financial support from NSF (CHE-2102609) and MRC for equipment usage. The computational resources were provided by Missouri S&T and by the NSF-MRI program (grant OAC-1919789).

REFERENCES

- (1) Whipple, D. T.; Kenis, P. J. A. Prospects of CO2 Utilization via Direct Heterogeneous Electrochemical Reduction. *J. Phys. Chem. Lett.* **2010**, *1*, 3451–3458.
- (2) Duan, X.; Xu, J.; Wei, Z.; Ma, J.; Guo, S.; Wang, S.; Liu, H.; Dou, S. Metal-Free Carbon Materials for CO2 Electrochemical Reduction. *Adv. Mater.* **2017**, *29*, No. 1701784.
- (3) Singh, H.; Bernabe, J.; Chern, J.; Nath, M. Copper Selenide as Multifunctional Non-Enzymatic Glucose and Dopamine Sensor. *J. Mater. Res.* **2021**, *36*, 1413–1424.
- (4) Singh, H.; Marley-Hines, M.; Chakravarty, S.; Nath, M. Multi-Walled Carbon Nanotube Supported Manganese Selenide as Highly

- Active Bifunctional OER and ORR Electrocatalyst. J. Mater. Chem. A 2022, 10, 6772–6784.
- (5) Gonglach, S.; Paul, S.; Haas, M.; Pillwein, F.; Sreejith, S. S.; Barman, S.; De, R.; Müllegger, S.; Gerschel, P.; Apfel, U. P.; Coskun, H.; Aljabour, A.; Stadler, P.; Schöfberger, W.; Roy, S. Molecular Cobalt Corrole Complex for the Heterogeneous Electrocatalytic Reduction of Carbon Dioxide. *Nat. Commun.* **2019**, *10*, 3864.
- (6) Su, P.; Iwase, K.; Harada, T.; Kamiya, K.; Nakanishi, S. Covalent Triazine Framework Modified with Coordinatively-Unsaturated Co or Ni Atoms for CO2 Electrochemical Reduction. *Chem. Sci.* **2018**, *9*, 3941–3947.
- (7) Sonoyama, N.; Kirii, M.; Sakata, T. Electrochemical Reduction of CO2 at Metal-Porphyrin Supported Gas Diffusion Electrodes under High Pressure CO2. *Electrochem. Commun.* **1999**, *1*, 213–216.
- (8) Mistry, H.; Varela, A. S.; Bonifacio, C. S.; Zegkinoglou, I.; Sinev, I.; Choi, Y. W.; Kisslinger, K.; Stach, E. A.; Yang, J. C.; Strasser, P.; Cuenya, B. R. Highly Selective Plasma-Activated Copper Catalysts for Carbon Dioxide Reduction to Ethylene. *Nat. Commun.* **2016**, *7*, 1–9.
- (9) Hori, Y.; Kikuchi, K.; Suzuki, S. Production of CO and CH₄ in electrochemical reduction of CO₂ at metal electrodes in aqueous hydrogencarbonate solution. *Chem. Lett.* **1985**, *14*, 1695–1698.
- (10) Saxena, A.; Liyanage, W.; Masud, J.; Kapila, S.; Nath, M. Selective Electroreduction of CO2 to Carbon-Rich Products by Simple Binary Copper Selenide Electrocatalyst. *J. Mater. Chem. A* **2021**, *9*, 7150.
- (11) Nath, M.; Singh, H.; Saxena, A. Progress of Transition Metal Chalcogenides as Efficient Electrocatalysts for Energy Conversion. *Curr. Opin. Electrochem.* **2022**, 34, No. 100993.
- (12) De Gregorio, G. L.; Burdyny, T.; Loiudice, A.; Iyengar, P.; Smith, W. A.; Buonsanti, R. Facet-Dependent Selectivity of Cu Catalysts in Electrochemical CO2 Reduction at Commercially Viable Current Densities. ACS Catal. 2020, 10, 4854–4862.
- (13) Li, Y.; Cui, F.; Ross, M. B.; Kim, D.; Sun, Y.; Yang, P. Structure-Sensitive CO2 Electroreduction to Hydrocarbons on Ultrathin 5-Fold Twinned Copper Nanowires. *Nano Lett.* **2017**, *17*, 1312–1317.
- (14) Liu, S.; Huang, S. Size Effects and Active Sites of Cu Nanoparticle Catalysts for CO 2 Electroreduction. *Appl. Surf. Sci.* **2019**, 475, 20–27.
- (15) Chen, K.; Ling, J.; Wu, C. In Situ Generation and Stabilization of Accessible Cu/Cu $_2$ O Heterojunctions inside Organic Frameworks for Highly Efficient Catalysis. *Angew. Chem., Int. Ed.* **2020**, *59*, 1925–1931.
- (16) Lin, S. C.; Chang, C. C.; Chiu, S. Y.; Pai, H. T.; Liao, T. Y.; Hsu, C. S.; Chiang, W. H.; Tsai, M. K.; Chen, H. M. Operando Time-Resolved X-Ray Absorption Spectroscopy Reveals the Chemical Nature Enabling Highly Selective CO2 Reduction. *Nat. Commun.* **2020**, *11*, 3525.
- (17) Singh, A. K.; Mukherjee, R. Cobalt(Ii) and Cobalt(Iii) Complexes of Thioether-Containing Hexadentate Pyrazine Amide Ligands: C–S Bond Cleavage and Cyclometallation Reaction. *J. Chem. Soc., Dalton Trans.* **2008**, *2*, 260–270.
- (18) Nath, M.; De Silva, U.; Singh, H.; Perkins, M.; Liyanage, W. P. R.; Umapathi, S.; Chakravarty, S.; Masud, J. Cobalt Telluride: A Highly Efficient Trifunctional Electrocatalyst for Water Splitting and Oxygen Reduction. *ACS Appl. Energy Mater.* **2021**, *4*, 8158–8174.
- (19) Sheng, H.; Frei, H. Direct Observation by Rapid-Scan FT-IR Spectroscopy of Two-Electron-Reduced Intermediate of Tetraaza Catalyst [CoIIN4H(MeCN)]2+ Converting CO2 to CO. *J. Am. Chem. Soc.* **2016**, *138*, 9959–9967.
- (20) Iablokov, V.; Beaumont, S. K.; Alayoglu, S.; Pushkarev, V. V.; Specht, C.; Gao, J.; Alivisatos, A. P.; Kruse, N.; Somorjai, G. A. Size-Controlled Model Co Nanoparticle Catalysts for CO 2 Hydrogenation: Synthesis, Characterization, and Catalytic Reactions. *Nano Lett.* **2012**, 12, 3091–3096.
- (21) Bernal, M.; Bagger, A.; Scholten, F.; Sinev, I.; Bergmann, A.; Ahmadi, M.; Rossmeisl, J.; Cuenya, B. R. CO2 Electroreduction on Copper-Cobalt Nanoparticles: Size and Composition Effect. *Nano Energy* **2018**, *53*, 27–36.
- (22) Nafria, R.; Genç, A.; Ibáñez, M.; Arbiol, J.; Ramírez De La Piscina, P.; Homs, N.; Cabot, A. Co-Cu Nanoparticles: Synthesis by Galvanic Replacement and Phase Rearrangement during Catalytic Activation. *Langmuir* **2016**, *32*, 2267–2276.

- (23) Gao, S.; Lin, Y.; Jiao, X.; Sun, Y.; Luo, Q.; Zhang, W.; Li, D.; Yang, J.; Xie, Y. Partially Oxidized Atomic Cobalt Layers for Carbon Dioxide Electroreduction to Liquid Fuel. *Nature* **2016**, *529*, 68–71.
- (24) Yu, H.; Cao, D.; Fisher, A.; Johnston, R. L.; Cheng, D. Size Effect on the Adsorption and Dissociation of CO 2 on Co Nanoclusters. *Appl. Surf. Sci.* **2017**, *396*, 539–546.
- (25) Mu, Q.; Zhu, W.; Yan, G.; Lian, Y.; Yao, Y.; Li, Q.; Tian, Y.; Zhang, P.; Deng, Z.; Peng, Y. Activity and Selectivity Regulation through Varying the Size of Cobalt Active Sites in Photocatalytic CO2 Reduction. *J. Mater. Chem. A* **2018**, *6*, 21110–21119.
- (26) Wannakao, S.; Jumpathong, W.; Kongpatpanich, K. Tailoring Metalloporphyrin Frameworks for an Efficient Carbon Dioxide Electroreduction: Selectively Stabilizing Key Intermediates with H-Bonding Pockets. *Inorg. Chem.* **2017**, *56*, 7200–7209.
- (27) Kresse, G.; Hafner, J. Ab Initio Molecular Dynamics for Liquid Metals. *Phys. Rev. B* **1993**, 47, 558–561.
- (28) Kresse, G.; Hafner, J. Ab Initio Molecular-Dynamics Simulation of the Liquid-Metal—Amorphous-Semiconductor Transition in Germanium. *Phys. Rev. B* **1994**, *49*, 14251–14269.
- (29) Kresse, G.; Furthmüller, J. Efficient Iterative Schemes for Ab Initio Total-Energy Calculations Using a Plane-Wave Basis Set. *Phys. Rev. B: Condens. Matter Mater. Phys.* **1996**, *54*, 11169–11186.
- (30) Kresse, G.; Furthmüller, J. Efficiency of Ab-Initio Total Energy Calculations for Metals and Semiconductors Using a Plane-Wave Basis Set. *Comput. Mater. Sci.* **1996**, *6*, 15–50.
- (31) Perdew, J. P.; Burke, K.; Ernzerhof, M. Generalized Gradient Approximation Made Simple. *Phys. Rev. Lett.* **1996**, *77*, 3865–3868.
- (32) Perdew, J. P.; Burke, K.; Ernzerhof, M. Erratum: Generalized Gradient Approximation Made Simple. *Phys. Rev. Lett.* **1997**, 78, 1396–1306
- (33) Blöchl, P. E. Projector Augmented-Wave Method. *Phys. Rev. B* **1994**, *50*, 17953–17979.
- (34) Joubert, D. From Ultrasoft Pseudopotentials to the Projector Augmented-Wave Method. *Phys. Rev. B: Condens. Matter Mater. Phys.* 1999, 59, 1758–1775.
- (35) Holzwarth, U.; Gibson, N. The Scherrer Equation versus the "Debye-Scherrer Equation.". *Nat. Nanotechnol.* **2011**, *6*, 534.
- (36) Yang, H.; Kubler, D. K.; Lavina, B.; Downs, R. T.; Costin, G. Tyrrellite, $Cu(Co_{0.68}Ni_{0.32})_2Se_4$, isostructural with spinel. *Acta Crystallogr.* **2007**, *C63*, i73–i74.
- (37) Masud, J.; Swesi, A. T.; Liyanage, W. P. R.; Nath, M. Cobalt Selenide Nanostructures: An Efficient Bifunctional Catalyst with High Current Density at Low Coverage. *ACS Appl. Mater. Interfaces* **2016**, *8*, 17292–17302.
- (38) Masud, J.; Liyanage, W. P. R.; Cao, X.; Saxena, A.; Nath, M. Copper Selenides as High-Efficiency Electrocatalysts for Oxygen Evolution Reaction. *ACS Appl. Energy Mater.* **2018**, *1*, 4075–4083.
- (39) Chauhan, M.; Reddy, K. P.; Gopinath, C. S.; Deka, S. Copper Cobalt Sulfide Nanosheets Realizing a Promising Electrocatalytic Oxygen Evolution Reaction. *ACS Catal.* **2017**, *7*, 5871–5879.
- (40) Cao, X.; Medvedeva, J. E.; Nath, M. Copper Cobalt Selenide as a High-Efficiency Bifunctional Electrocatalyst for Overall Water Splitting: Combined Experimental and Theoretical Study. ACS Appl. Energy Mater. 2020, 3, 3092–3103.
- (41) Clark, E. L.; Resasco, J.; Landers, A.; Lin, J.; Chung, L. T.; Waltin, A.; Hahn, C.; Jaramilo, T. F.; Bell, A. T. Standards and protocols for data acquisition and reporting for studies of the electrochemical reduction of carbon dioxide. *ACS Catal.* **2018**, *8*, 6560–6570.
- (42) Yu, Y.; Zhong, N.; Fang, J.; Tang, S.; Ye, X.; He, Z.; Song, S. Comparative Study between Pristine Ag and Ag Foam for Electrochemical Synthesis of Syngas with Carbon Dioxide and Water. *Catalysts* **2019**, *9*, 57.
- (43) Sun, Z.; Ma, T.; Tao, H.; Fan, Q.; Han, B. Fundamentals and Challenges of Electrochemical CO2 Reduction Using Two-Dimensional Materials. *Chem* **2017**, *3*, 560–587.
- (44) Dong, X.; Yu, Y.; Jing, X.; Jiang, H.; Hu, T.; Meng, C.; Huang, C.; Zhang, Y. Sandwich-like Honeycomb Co2SiO4/RGO/Honeycomb Co2SiO4 Structures with Enhanced Electrochemical Properties for

- High-Performance Hybrid Supercapacitor. J. Power Sources 2021, 492, No. 229643.
- (45) Boggio, R.; Carugati, A.; Trasatti, S. Electrochemical surface properties of Co₃O₄ electrodes. *J. Appl. Electrochem.* **1987**, *17*, 828–840.
- (46) Li, M.; Zhang, J.-Y.; Zhang, Y.; Wang, T.-M. A Density Functional Theory Study on the Adsorption of CO and O2 on Cu-Terminated Cu2O (111) Surface. *Chin. Phys. B* **2012**, *21*, No. 067302.
- (47) Yadav, V. S. K.; Purkait, M. K. Electrochemical Studies for CO2 Reduction Using Synthesized Co3O4 (Anode) and Cu2O (Cathode) as Electrocatalysts. *Energy Fuels* **2015**, *29*, 6670–6677.
- (48) Kuhl, K. P.; Cave, E. R.; Abram, D. N.; Jaramillo, T. F. New Insights into the Electrochemical Reduction of Carbon Dioxide on Metallic Copper Surfaces. *Energy Environ. Sci.* **2012**, *5*, 7050–7059.
- (49) Cave, E. R.; Montoya, J. H.; Kuhl, K. P.; Abram, D. N.; Hatsukade, T.; Shi, C.; Hahn, C.; Nørskov, J. K.; Jaramillo, T. F. Electrochemical CO2 Reduction on Au Surfaces: Mechanistic Aspects Regarding the Formation of Major and Minor Products. *Phys. Chem. Chem. Phys.* **2017**, *19*, 15856–15863.
- (50) Hori, Y. Electrochemical CO2 Reduction on Metal Electrodes. In *Modern Aspects of Electrochemistry*; Springer: New York, 2008; pp 89–189.
- (51) Patra, A.; Peng, H.; Sun, J.; Perdew, J. P. Rethinking CO Adsorption on Transition-Metal Surfaces: Effect of Density-Driven Self-Interaction Errors. *Phys. Rev. B* **2019**, *100*, No. 035442.
- (52) Christmann, K.; Schober, O.; Ertl, G. Adsorption of CO on a Ni(111) Surface. J. Chem. Phys. 2003, 60, 4719.
- (53) Qiu, W.; Liang, R.; Luo, Y.; Cui, G.; Qiu, J.; Sun, X. A Br—anion adsorbed porous Ag nanowire film: in situ electrochemical preparation and application toward efficient CO2 electroreduction to CO with high selectivity. *Inorg. Chem. Front.* **2018**, *5*, 2238–2241.